

Simulations of DNA stretching by flow field in microchannels with complex geometry

Chiou-De Huang, Dun-Yen Kang, and Chih-Chen Hsieh

Citation: *Biomicrofluidics* **8**, 014106 (2014); doi: 10.1063/1.4863802

View online: <http://dx.doi.org/10.1063/1.4863802>

View Table of Contents: <http://scitation.aip.org/content/aip/journal/bmf/8/1?ver=pdfcov>

Published by the [AIP Publishing](#)

Articles you may be interested in

Stretching DNA by electric field and flow field in microfluidic devices: An experimental validation to the devices designed with computer simulations

Biomicrofluidics **7**, 014109 (2013); 10.1063/1.4790821

Simulation guided design of a microfluidic device for electrophoretic stretching of DNA

Biomicrofluidics **6**, 044105 (2012); 10.1063/1.4763559

An immersed boundary method for Brownian dynamics simulation of polymers in complex geometries: Application to DNA flowing through a nanoslit with embedded nanopits

J. Chem. Phys. **136**, 014901 (2012); 10.1063/1.3672103

Electrical detection of DNA immobilization and hybridization by streaming current measurements in microchannels

Appl. Phys. Lett. **99**, 183702 (2011); 10.1063/1.3658457

Precise DNA placement and stretching in electrode gaps using electric fields in a microfluidic system

Appl. Phys. Lett. **90**, 083901 (2007); 10.1063/1.2535556



AIP | **APL Photonics**

APL Photonics is pleased to announce
Benjamin Eggleton as its Editor-in-Chief



Simulations of DNA stretching by flow field in microchannels with complex geometry

Chiou-De Huang, Dun-Yen Kang, and Chih-Chen Hsieh^{a)}

Department of Chemical Engineering, National Taiwan University, Taipei 106, Taiwan

(Received 17 December 2013; accepted 20 January 2014; published online 7 February 2014)

Recently, we have reported the experimental results of DNA stretching by flow field in three microchannels (C. H. Lee and C. C. Hsieh, *Biomicrofluidics* 7(1), 014109 (2013)) designed specifically for the purpose of preconditioning DNA conformation for easier stretching. The experimental results do not only demonstrate the superiority of the new devices but also provides detailed observation of DNA behavior in complex flow field that was not available before. In this study, we use Brownian dynamics-finite element method (BD-FEM) to simulate DNA behavior in these microchannels, and compare the results against the experiments. Although the hydrodynamic interaction (HI) between DNA segments and between DNA and the device boundaries was not included in the simulations, the simulation results are in fairly good agreement with the experimental data from either the aspect of the single molecule behavior or from the aspect of ensemble averaged properties. The discrepancy between the simulation and the experimental results can be explained by the neglect of HI effect in the simulations. Considering the huge savings on the computational cost from neglecting HI, we conclude that BD-FEM can be used as an efficient and economic designing tool for developing new microfluidic device for DNA manipulation. © 2014 AIP Publishing LLC. [<http://dx.doi.org/10.1063/1.4863802>]

INTRODUCTION

With the advance of single-molecule techniques over the past decade, the behavior of macromolecules has been intensively investigated through experiments that were not possible before. These studies started from investigating the fundamental behavior of macromolecules in bulk space.^{2–9} Later, the influence of various types of confinement to the static and dynamic properties of macromolecules has also been studied.^{10–18} Their results did not only examine the predictions made in literatures but also revealed many phenomena that were not expected before. The majority of these studies have used DNA as the representative macromolecules because fluorescently labeled DNA can be easily visualized by using optical microscopy. Therefore, these studies have provided visual observation of detailed molecular behavior as well as direct measurement of many interested properties. The even more important reason for using DNA is due to its own importance as the core material of inheritance. It is hoped that deeper understanding of DNA behavior and its interactions with the environment can inspire new applications that would allow DNA to be more easily manipulated and more efficiently analyzed.

With accumulated experimental results, the development of simulation techniques to model DNA behavior has also received more attention. The simulations were first used in order to qualitatively understand the underlying physics of DNA behavior.^{19–26} Through the comparison with experimental data, the capability and the limitation of various models and simulation methods were also revealed. From comparing the experimental and simulated DNA behavior in simple geometry, it is the hope that the simulation techniques can be refined and eventually be

^{a)} Author to whom correspondence should be addressed. Electronic mail: ccjhsieh@ntu.edu.tw

used as design tools for developing the future applications involving manipulating DNA in complex geometry.

To simulate accurately DNA behavior in fluid, it requires the ability to correctly describe both the elasticity of DNA and the interaction between fluid and DNA. In other words, a model for DNA and a model for fluid have to be properly chosen and coupled together. For modeling DNA conformation and elasticity at mesoscopic and macroscopic level, the coarse-grained bead-spring and bead-rod model²⁷ have been shown capable of reproducing DNA behavior. Consequently, these two models have been the dominant choices for simulating DNA. The more difficult part, however, is to model the fluid and its interaction with DNA. To model the fluid, different approaches are available with their own strengths and weaknesses. The classical approach is to treat fluid as continuum and to solve the Navier-Stokes equation to obtain the flow field. If analytical solution is not available, numerical solution obtained using computational fluid dynamics can be used instead.^{28,29} The information of the flow field is then fed into the Brownian dynamics (BD) simulation to describe the motion of DNA. This approach is computationally more affordable than those with more detailed fluid models. However, since it treats the fluid and imbedded macromolecules independently, the effect of hydrodynamic interaction (HI) is not naturally included. A remedy for low Reynolds number condition is to use the so called “HI tensor”^{19,27} that accounts for the HI effect through an anisotropic, conformation-dependent drag force. Although this method to include HI in BD has been shown to work very well^{19–21,28,30–32} as long as an appropriate description of HI tensor is available, using HI tensor in BD simulations is computationally very expensive. Moreover, the analytical or approximated formula³³ of HI tensor is only available for few very simple geometries.^{34–36} Mesoscopic fluid models such as Lattice Boltzmann methods (LB)³⁷ and stochastic rotational dynamics³⁸ (SRD) (or its close variation multi-particle collision dynamics (MPCD))^{39,40} are potential candidates to overcome this problem. Several studies have employed the coarse-grained polymer models with mesoscopic fluid models to predict DNA behavior in simple confined geometry and obtained satisfactory results in comparison with the experimental data.^{41–43} Although these methods are possible to be used for modeling fluid problem in complex geometries, they have to discretize the space into small lattices or cells with the size determined by the smallest feature of the geometry. Consequently, applying these methods to complex geometries, especially those with high aspect ratio, can become prohibitively expensive.

Because of the limit in computational cost, Brownian dynamics has been the only method so far used to predict DNA behavior in real devices with non-trivial geometry.^{44,45} The majority of these studies have focused on predicting the electrophoretic motion of DNA, and they essentially fall into two categories: separation of DNA through a post array^{29,46–49} and stretching DNA^{44,50–52} for rapid gene analysis. Since these studies were inspired by gel electrophoresis⁵³ and it is also very easy to apply electric field in experiments, driving DNA electrophoretically has been the most popular means for manipulating DNA. Although not including HI, BD-FEM have been extensively used to model these experiments and shown to be capable of giving semi-quantitative agreement with experimental data.⁵² With these successful experiences, several studies have tried to use BD-FEM to help design better devices.^{54–57} On the other hand, flow field has rarely been used as the driving force to operate these devices. This situation may change in the future because DNA was found to behave very differently under moderate to high electric field,^{1,58} limiting the possibility of more efficient operation. Therefore, evaluating the accuracy of BD-FEM simulations for predicting DNA behavior in complex flow field is needed.

However, some subtle but important differences exist between modeling DNA in electric field and in flow field. First, HI effect is much weakened in electric field since the DNA motion caused by the electric field does not induce HI.^{29,59} Therefore, although HI caused by the nonelectrical forces still exists, it is much diminished and only has insignificant influence on DNA behavior. Second, DNA in electric field experiences an irrotational flow-like field which is purely extensional or compressional, resulting in a shearless field. In flow field, the no-slip boundary condition must be fulfilled at all solid boundaries, and thus the flow field often has a strong shear component that has important but complicate influence on DNA behavior.

In literatures, we find that very few studies^{28,32,36,60,61} have compared simulated DNA behavior in complex flow field with experimental observation. The reason of such few studies available is mainly due to the lack of experimental results to compare with. Among these studies, only the work of Teclemariam *et al.*⁶¹ has made detailed comparison at single molecule level. They compared DNA dynamics in post arrays under flow field from experiments and simulations. The simulations were performed using BD-FEM with bead-rod model, and the HI effect was not included. Also, since the posts are very tall relative to their diameter, the flow field was modeled as 2-dimensional field. Although not considering HI, the simulation results were in very good agreement with experimental data. Therefore, it was concluded that BD simulations without HI can be used to guide the future design of post arrays for DNA separation.

In our previous study,¹ we have performed T4-DNA stretching experiments by flow field in three microfluidic devices with complex shapes. Figs. 1(a)–1(c) show the shape and the design parameters of the three devices. We note that all three devices have the uniform height of $2\ \mu\text{m}$, but their widths are varying between $1.9\ \mu\text{m}$ and $200\ \mu\text{m}$. Different from the study of Teclemariam *et al.*,⁶¹ the flow field in our devices is more complex because it is fully 3-dimensional. From this point of view, our experiments have provided a unique chance to evaluate the performance of current simulation techniques under the most realistic situation. In this study, we shall use BD-FEM method to simulate DNA in the devices. Although we realize the importance of HI, we do not have affordable solution for the current case and therefore HI is not included in our simulations. We hope that this study can give us an idea about how much we can trust the BD-FEM results for future device design and how HI quantitatively affects DNA behavior in real complex flow field.

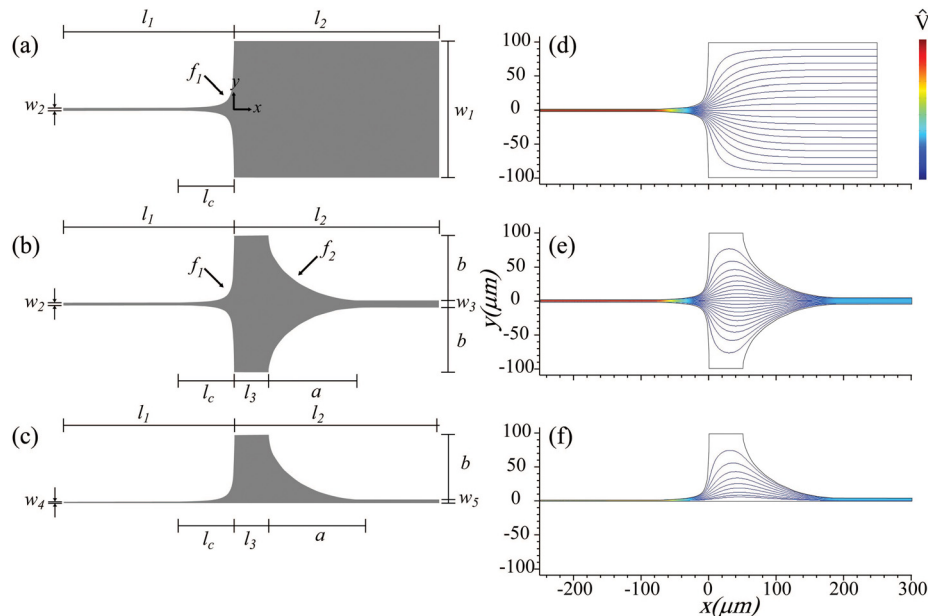


FIG. 1. The schematic diagram of the devices. (a) Case I: contraction only, (b) Case II: contraction with an expansion for pre-stretching DNA, (c) Case III: Case II cut to half along $y = 0$, a modification of case II to prevent DNA from passing the region near the axis of case II. (d), (e) and (f) show the representative streamlines in case I, case II and case III, respectively. The design parameters are listed below: $w_1 = 200\ \mu\text{m}$, $w_2 = 3.8\ \mu\text{m}$, $w_3 = 10\ \mu\text{m}$, $w_4 = 1.9\ \mu\text{m}$, $w_5 = w_3/2 = 5\ \mu\text{m}$, $l_1 = 250\ \mu\text{m}$, $l_2 = 300\ \mu\text{m}$, $l_3 = 50\ \mu\text{m}$, the contraction length $l_c = 80\ \mu\text{m}$, $a = 140\ \mu\text{m}$, $b = 95\ \mu\text{m}$, $f_1 = \frac{w_1}{2(\frac{w_1}{w_2} - 1) + 1}$; $f_2 = 100 - b\sqrt{1 - \frac{(190-x)^2}{a^2}}$. The height h of all three devices is $2\ \mu\text{m}$ in z direction. The origin and the direction of x and y directions are defined in (a). The definition of z direction (not shown) follows the right-hand rule and its origin is set at the bottom surface of the devices. When these devices operate, DNA molecules are driven from the inlet (right) to the outlet (left).

SIMULATION METHODS

The two main parts of our simulation method are Finite element calculation of the flow field and Brownian dynamics simulations for describing DNA motion. The flow field was obtained first and fed as input data to Brownian dynamics simulations. As stressed in the previous section, the hydrodynamic interaction due to DNA motion was neglected in our simulations. The shape and the design parameters of the devices are given in Fig. 1. The real devices have very long inlet channel, but we have neglected those parts in our simulations to make simulations affordable. The governing equations for the flow field \mathbf{V} are the Stokes equations:

$$-\nabla p + \mu \nabla^2 \mathbf{V} = 0, \quad (1)$$

where p is pressure, μ is viscosity. The no-slip boundary condition was set to all solid boundaries. The boundary condition for pressure is set to $p=0$ at the outlet and $p=p_{\text{given}}$ at the inlet of the devices. Here p_{given} is chosen so that the resulting velocity field gradient matches the desired Deborah number (De). The velocity field \mathbf{V} was solved using FEM solver with tetrahedral elements. The solved velocity profile at the inlet and the outlet of the devices where the channels are rectangular was compared with the analytical solutions to ensure the accuracy of our numerical solutions. Once the velocity on the nodes is solved, \mathbf{V} at any place in the device can be calculated from the interpolation of 10-node P_2^0 shape function. The connection between FEM data and BD simulations is established with an efficient searching algorithm developed in our previous study.⁵⁵

The dynamics of DNA in the flow field is simulated using Brownian dynamics with the bead-spring model which contains N_b beads connected by $N_s (= N_b - 1)$ springs. To match the experimental condition, stained T4-DNA with contour length L of $70 \mu\text{m}$ was modeled by a 63-bead chain. The force balance on each bead leads to the equation of the evolution of bead position:

$$\frac{d\mathbf{r}_i}{dt} = \mathbf{V}(\mathbf{r}_i) + \frac{1}{\zeta} \left[\mathbf{F}_i^B(t) + \mathbf{F}_i^S(t) + \mathbf{F}_i^{EV}(t) + \mathbf{F}_i^{EV,wall}(t) \right], \quad (2)$$

where \mathbf{r}_i is the position of i -th bead, $\mathbf{V}(\mathbf{r}_i)$ is the flow velocity at \mathbf{r}_i , ζ is the drag coefficient of a bead, \mathbf{F}_i^B is the Brownian force, \mathbf{F}_i^S is the sum of the spring forces acting on the i -th bead, \mathbf{F}_i^{EV} is the sum of the excluded volume force between the beads, and $\mathbf{F}_i^{EV,wall}$ is the excluded volume force between the i -th bead and the wall. To perform BD simulations, Eq. (2) was made dimensionless with the following dimensionless variables:

$$\hat{\mathbf{r}} \equiv \frac{\mathbf{r}}{l}, \quad \hat{t} \equiv \frac{t}{\zeta l^2 / k_B T}, \quad \hat{\mathbf{V}} \equiv \frac{\mathbf{V}}{V_0}, \quad \hat{\mathbf{F}}(\hat{\mathbf{r}}) \equiv \frac{\mathbf{F}(\mathbf{r})l}{k_B T}, \quad (3)$$

where l is the maximum extension of a spring ($=L/N_s$), $k_B T$ is the thermal energy, and V_0 is the average velocity at the inlet of case I. Substituting Eq. (3) into Eq. (2), the dimensionless equation of motion is obtained as

$$\frac{d\hat{\mathbf{r}}_i}{d\hat{t}} = Pe \hat{\mathbf{V}}(\hat{\mathbf{r}}_i) + \hat{\mathbf{F}}_i^B + \hat{\mathbf{F}}_i^S + \hat{\mathbf{F}}_i^{EV} + \hat{\mathbf{F}}_i^{EV,wall}, \quad (4)$$

where $Pe = \mu^b V_0 l / D$ is the bead Peclet number, D is the diffusivity of a bead ($=k_B T / \zeta$). The dimensionless Brownian force term $\hat{\mathbf{F}}_i^B$ is described by

$$\hat{\mathbf{F}}_i^B = \sqrt{\frac{6}{\delta \hat{t}}} \mathbf{R}_i, \quad (5)$$

where \mathbf{R}_i is a vector with each of its three components uniformly distributed between -1.0 and 1.0 . The spring force between beads i and j , $\hat{\mathbf{f}}_{ij}^S$, is described by a modified Marko-Siggia spring law derived by Underhill and Doyle:⁶²

$$\hat{\mathbf{f}}_{i,j}^S = \frac{\nu}{\lambda} \left\{ \hat{r}_{ji} - \frac{1}{4} + \frac{1}{4(1 - \hat{r}_{ji})^2} \right\} \frac{\hat{\mathbf{r}}_j - \hat{\mathbf{r}}_i}{\hat{r}_{ji}}, \quad (6)$$

where \hat{r}_{ji} is the dimensionless distance between beads i and j , $\nu(\equiv l/A_p)$ is the number of the true persistence length A_p per spring, and $\lambda(\equiv A_{eff}/A_p)$ is the ratio of the effective persistence length to the true DNA persistence length. In this study, A_p is set to $0.053 \mu\text{m}$, and therefore $\nu = 21.3$. A_{eff} is set to be $0.07362 \mu\text{m}$, slightly longer than A_p so that the additional flexibility caused by the discretization of a DNA into a bead-spring chain can be offset.^{62,63} Since each bead is connected by either one or two springs, the total spring force acting on bead i depends on its position in the chain:

$$\hat{\mathbf{F}}_i^S = \begin{cases} \hat{\mathbf{f}}_{i,i+1}^S & i = 1 \\ \hat{\mathbf{f}}_{i,i+1}^S + \hat{\mathbf{f}}_{i,i-1}^S & 1 < i < N_b. \\ \hat{\mathbf{f}}_{i,i-1}^S & i = N_b. \end{cases} \quad (7)$$

The excluded volume effect between DNA segments is modeled by a soft repulsive potential between beads,⁶⁴ and the dimensionless excluded volume force acting on bead i , $\hat{\mathbf{F}}_i^{EV}$, is expressed as follows:

$$\hat{\mathbf{F}}_i^{EV} = - \sum_{j=1(j \neq i)}^{N_b} \frac{9}{2} \hat{v}^{EV,p} \left(\frac{3}{4\sqrt{\pi}} \right)^3 \nu^{\frac{9}{2}} \exp\left(\frac{-9\nu\hat{r}_{ji}^2}{4} \right) \hat{\mathbf{r}}_{ji}, \quad (8)$$

where $\hat{v}^{EV,p}(=v^{EV,p}/l^3)$ is the dimensionless excluded volume parameter, and its dimensional value of $v^{EV,p}$ is set to $0.0004 \mu\text{m}^3$. This potential has been shown to produce correct dependence between DNA contour length and its equilibrium size under good-solvent condition. The simulated bulk radius of gyration ($R_{g,bulk}$) of DNA is $1.44 \mu\text{m}$, in agreement the value reported in experiments¹⁰ and simulations.⁵⁴

A bead-wall repulsive potential is employed to prevent bead from penetrating the wall of the device:³¹

$$U_i^{wall} = \begin{cases} \frac{A_{wall}}{6A_p\delta_{wall}^2} (y - \delta_{wall})^3 & \text{for } y < \delta_{wall} \\ 0 & \text{for } y \geq \delta_{wall} \end{cases}, \quad (9)$$

where y is the distance between the i -th bead and the wall, A_{wall} is the energy barrier ($=25k_B T$) of the repulsive potential, and δ_{wall} ($=0.1729 \mu\text{m}$) is the cut-off distance of the potential. However, even with this repulsive potential on the wall, the beads still have chance to penetrate the wall. When this situation is encountered, the bead is moved back to the nearest wall, i.e., the so-called Heyes-Melrose algorithm.⁶⁵

Since the main DNA property measured from the experiments is the DNA extension L_{ex} versus its x -coordinate at various De , we iterate their definitions as follows. L_{ex} is defined as the distance between the maximum coordinates (x_{max} , y_{max}) and the minimum coordinates (x_{min} , y_{min}) of a DNA molecule, and the x -coordinate of a DNA is defined by its x_{min} . The definition of the characteristic De is the same as that used in the experimental study:¹ $De = \tau \dot{\epsilon} \approx \tau (\frac{v_{outlet}}{l_c})$. Here v_{outlet} is the average fluid velocity over the cross-section at the outlet of the contraction ($x = -80 \mu\text{m}$) and τ is the longest relaxation time of DNA simulated in a $2 \mu\text{m}$ high slit. To have good statistics, all the ensemble averaged results were obtained from 300 independent runs starting with different initial conformations pre-equilibrated with the flow condition in the inlet channel. The BD simulations were performed by integrating Eq. (4) with

an explicit Euler's method. The dimensionless time step δt was fixed to be 10^{-6} for $De \leq 10$. The time step size was adjusted by a factor $10/De$ for $De > 10$.

RESULTS AND DISCUSSIONS

Figs. 1(d)–1(f) give the representative streamlines obtained at the plane $z = 1 \mu\text{m}$ in the devices. Comparing with Fig. 5 of our previous study,⁵⁶ the shape of the streamlines and the electric field lines are very similar. Thus, DNA molecules should have similar trajectories when driven by either field. However, one of the major differences between the flow field and electric field is the shear component associated with flow field. Since all three devices are very shallow (the maximum width/height = 100), DNA always experiences a strong shear component in xz plane. Similar shear effect also appears near the side wall of the devices. In steady shear flow, the shear component has been shown to have multiple effects on DNA behavior, including pre-stretching, tumbling, and HI induced migration from solid boundary. Since the height of our devices is smaller than two times of the bulk radius of gyration of the DNA, HI induced DNA migration should be negligible in z direction. However, since the width of the devices is everywhere larger than the size of DNA molecules, HI induced DNA migration and depletion layer may become evident near the side walls.

To reveal more detailed flow condition in the devices, we present in Fig. 2 the velocity profile at (a) $x = 190 \mu\text{m}$, (b) $x = 130 \mu\text{m}$, (c) $x = 0 \mu\text{m}$ and (d) $x = -80 \mu\text{m}$, respectively. These four places correspond to the inlet region of all devices, the middle of the expansion of case II and case III, the inlet of the contraction channel and the outlet of the contraction channel for all three cases, respectively. In each subfigure, we present the contour plot of \hat{V}_x at yz plane and also its projection along $z = 1 \mu\text{m}$. As can be seen from Fig. 2(a), very strong shear flows appear near the side walls and near the top and the bottom walls in the inlet channels of case II

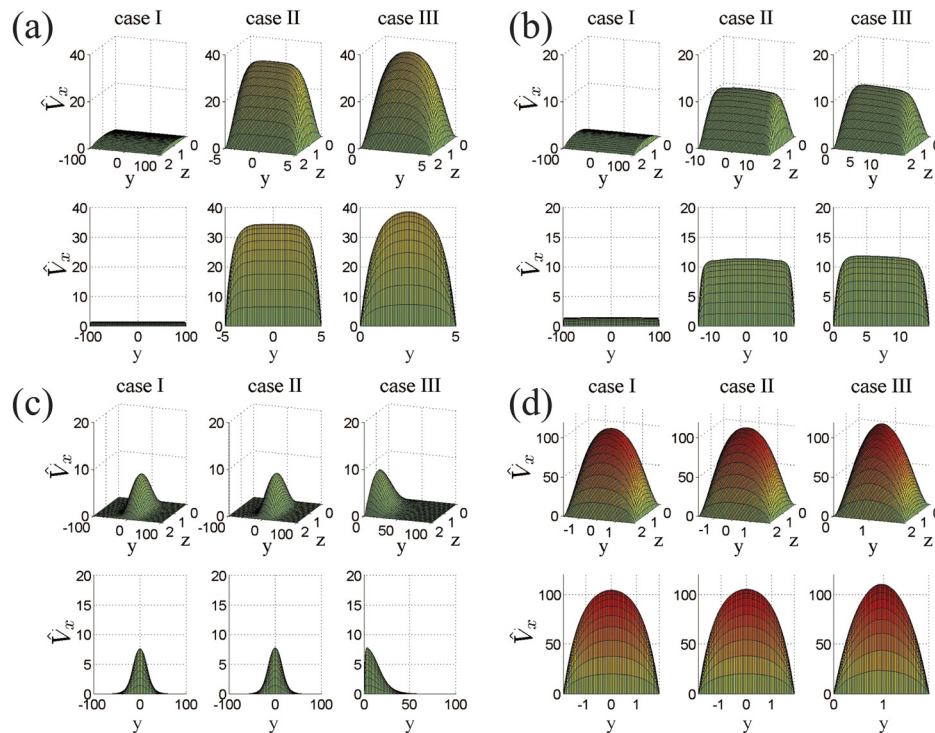


FIG. 2. The profile of dimensionless x -component of velocity (\hat{V}_x) at different cross-sections in the three devices at $De = 30$. (a) $x = 190 \mu\text{m}$ (at the inlet region of the devices). (b) $x = 130 \mu\text{m}$ (at the middle of the expansion of case II and case III). (c) $x = 0 \mu\text{m}$ (at the inlet of the contraction). (d) $x = -80 \mu\text{m}$ (at the outlet of the contraction). Each subfigure contains six plots where those in the top rows give the contour plot of \hat{V}_x and those in the bottom rows give the projection of \hat{V}_x at $z = 1 \mu\text{m}$ on the same cross-section.

and case III. In the expansion region (Fig. 2(b)), \hat{V}_x decreases with increasing channel width. This change weakens the shear component but also results in an extensional component in y direction that can stretch DNA. In the contraction (Figs. 2(c) and 2(d)), \hat{V}_x in all three cases accelerates greatly and results in a very strong extensional flow capable of stretching DNA there. Overviewing the velocity profile at different places, a general feature is that the shear component was always associated with the local flow field.

Fig. 3 compares the evolution patterns of T4-DNA from experiments ((a)–(e)) and simulations ((f)–(j)). Except that Figs. 3(e) and 3(j) were taken at $De = 30$, the rest were all taken at $De = 20$. Figs. 3(a) and 3(f) show the typical evolution pattern of T4-DNA in case I. The DNA molecules in both experiments and simulations were stretched only to a little extent before entering the contraction. Figs. 3(b) and 3(g) show that T4-DNA in case II undergo the characteristic extension-rotation motion^{55,56} in the expansion region of the device. This gives rise to the pre-conditioning effect that helps DNA to unravel at the expansion region and eventually reach higher extension in the contraction. Figs. 3(c) and 3(h) show another typical DNA evolution pattern often seen in case II. For DNA flowing near the center axis of case II, DNA in both experiments and simulations are stretched at the expansion but later adopt a folded conformation at the inlet of the contraction. This is due to the symmetric flow field on both sides of the center axis, as explained in details in our previous study.¹ Figs. 3(d) and 3(i) compare DNA behavior in case III. It is found that DNA also undergo the extension-rotation motion as seen in case II. However, because in case III a wall replaces the center axis of case II, the folded conformation shown in Figs. 3(c) and 3(h) does not form. At last, Figs. 3(e) and 3(j) compare the experimentally observed and simulated DNA behavior when they are moving very close to the side wall of the contraction channel at high De ($De = 30$). Fig. 3(e) shows that DNA in experiments experience the “flip motion”¹ in the very close vicinity of channel wall. As reported in experiments, the flip motion was sometimes observed for $De > 20$. However, the flip motion was never predicted in our simulations (Fig. 3(j)). We suspected that the absence of the flip motion in simulations may be due to the excluded volume effect imposed between DNA and the device wall. When we turned off the wall repulsive potential and only used the Heyes-Melrose algorithm, we sometimes did observe the flip motion of DNA, but we also found that DNA often move very slowly as they were very close to the walls. These slow-moving chains have never been observed in the experiments, but their appearance in our simulations strongly influences the qualitative feature of the averaged DNA extension. Thus, we speculate that DNA-wall interaction is much more subtle than the simple description used in our simulations. To summarize, our simulations reproduce all except one of the typical DNA evolution patterns found in experiments. The only DNA evolution pattern that was not predicted by our simulations should have little influence to the averaged DNA extension because it is seldom seen even in experiments.

Having the qualitative agreement between experiments and simulations, we present the quantitative comparison in the following sections. Figs. 4(a)–4(d) compare the evolution of DNA extension from experiments and simulations at $De = 5, 10, 20$, and 30 , respectively. Although a fully quantitative agreement has not been achieved, it is obvious that the simulations indeed capture all the qualitative features of experimental data. For example, in all three devices and at all four De , the simulated DNA extension starts to rise and reaches the maximum at the same positions as those observed in experiments. The agreement is especially apparent in Fig. 4(c) in which the experimental data was available over larger area of the devices and the comparison between experiments and simulations are the most complete. As can be seen in Fig. 4(c), DNA extension in the inlet channel ($x > 190 \mu\text{m}$) of case II and case III is nearly 40% from both the experiments and the simulations. The relative high extension of DNA was due to the strong shear component presented there. The fact that DNA in Case III extend more than those in case II is also consistent with the flow field given in Fig. 2(a) that the shear rate is higher in case III. The DNA extension in both cases then falls in the expansion region ($50 \mu\text{m} < x < 190 \mu\text{m}$) where the flow accelerates in y direction but slows down in x direction. Finally, DNA extension rises again when they move close to the inlet of the contraction ($x = 0 \mu\text{m}$) and reach the highest extension at $x \sim -96 \mu\text{m}$. Figs. 4(e)–4(l) provide the

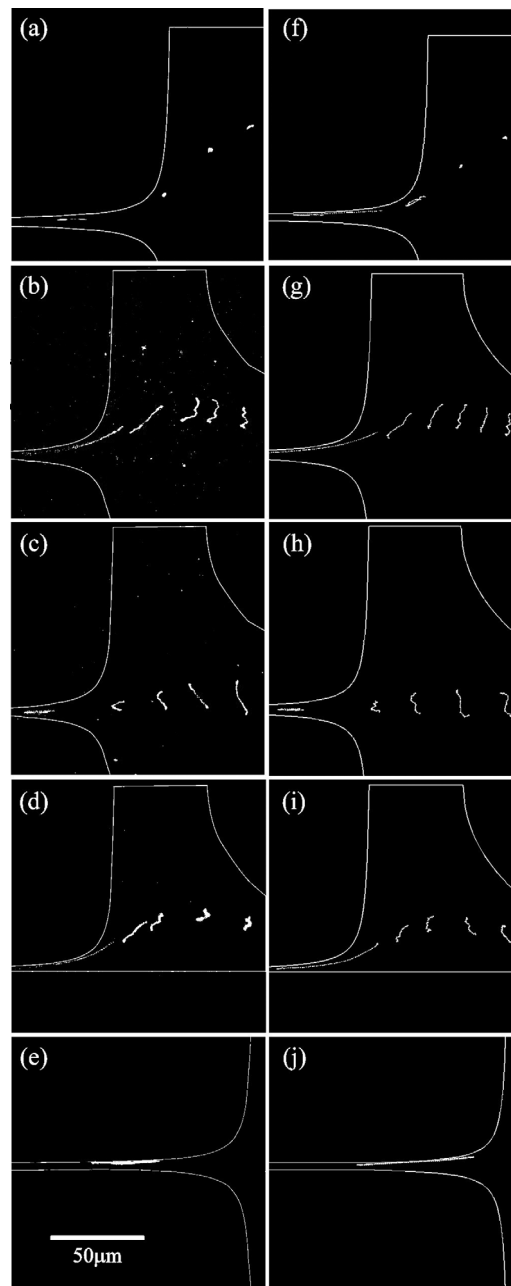


FIG. 3. Comparison of the evolution patterns of T4-DNA from experiments ((a)–(e)) and simulations ((f)–(j)). The flow direction is pointing from right to left. (a), (f) DNA in case I are stretched only after entering the contraction. (b), (g) DNA in case II undergo the extension-rotation motion that pre-conditions DNA for easier stretching in the contraction. (c), (h) DNA in case II were stretched at the expansion but later adopted a folded conformation at the inlet of the contraction. (d), (i) DNA in case III also undergoes the extension-rotation motion, (e) DNA undergoes the flip motion in the very close vicinity of channel wall, (j) the flip motion was never observed in the simulations. Except for (e) and (j) that were taken at $De = 30$, all the rest were taken at $De = 20$. (b) and (c) are reprinted with permission from Biomicrofluidics 7 (1), 014109 (2013). Copyright 2013 American Institute of Physics.

comparison of the probability distribution of DNA extension at the inlet of the contraction ($x = 0 \mu\text{m}$) and at the place where the averaged DNA extension reaches its maximum ($x \approx -96 \mu\text{m}$) at $De = 5, 10, 20$, and 30 , respectively. For $De = 5$, there were no experimental data available, so only the simulation results were presented. Again, the characteristic features of DNA extension distribution from experiments and simulations are in very good agreement.

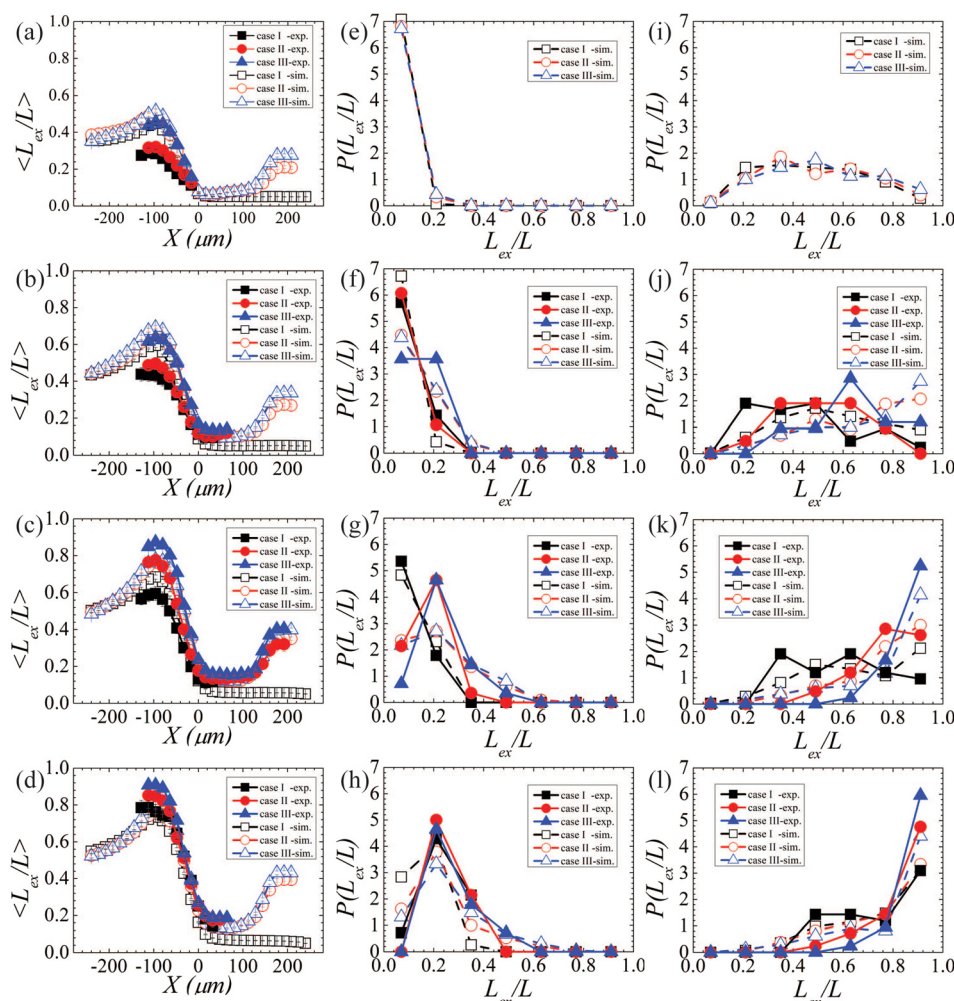


FIG. 4. Comparison of the ensemble averaged relative T4-DNA extension from simulations (hollow symbols and dashed lines) and from experiments (bold symbols and lines) at (a) $De = 5$, (b) $De = 10$, (c) $De = 20$, and (d) $De = 30$ in three devices. The probability distributions of the relative DNA extension from simulations are also compared with those from experiments at the inlet of the contraction ((e), (f), (g) and (h)) and at the place where the averaged DNA extension reaches its maximum ((i), (j), (k) and (l)).

Fig. 5 summarizes the simulated maximum relative DNA extension ($L_{ex,max}$) as a function of De , and compares it with the experimental data. The results of homogeneous field represent the theoretical limit of DNA extension at the corresponding De with infinite strain.⁶⁶ As can be seen, the simulated DNA extension improves with increasing De and seems to approach a plateau at high De . The simulations also predicted that at all De case III will slightly outperform case II, but case II will strongly outperform case I. The former prediction is somewhat different from our expectation based on the simulation results for electric field.⁵⁶ We expected that the shape of case III will prevent the formation of folded DNA that is frequently generated near the central axis of case II. However, it is found that although in simulations case III indeed prevented the formation of folded conformation as seen in Figs. 3(c) and 3(h), the slower velocity near the boundary leads to a locally lower De region and results in lower DNA extension in that area. Thus, in simulations, case III only performs slightly better than case II.

Comparing the simulation results with the experimental data, good qualitative agreement is accomplished again, but quantitative differences exist. We observed two trends in the deviation between experiments and simulations. First, the simulations tend to overpredict DNA extension at low De , while the deviation was reversed at high De . Second, the performance gap between case II and case III is much more significant than predicted by simulations. We believe that

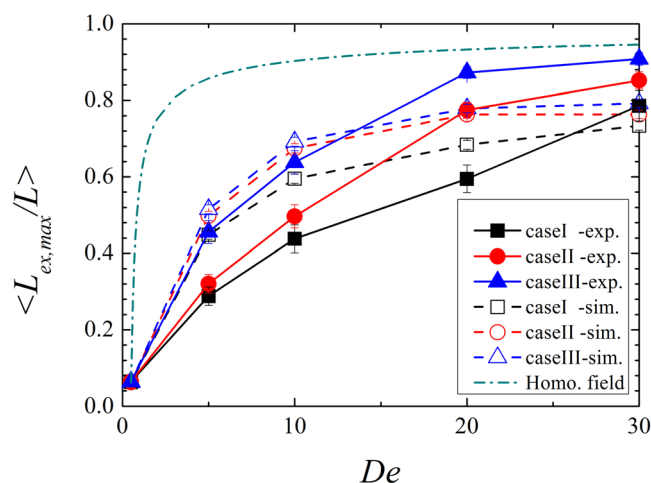


FIG. 5. The maximum ensemble averaged T4-DNA extension as a function of De . The bold symbols represent the experimental data from our previous study,¹ and the hollow symbols are the simulation results. The dashed-dotted line represents DNA extension estimated under a constant velocity gradient (infinite strain limit).

both trends were caused by the neglect of hydrodynamic interaction. The former can be explained by the intra-molecular hydrodynamic interaction while the latter is caused by the HI between DNA and the wall. To explain the first trend, we note that HI has opposite effects to the unraveling of a chain at the near-coil state and at more extended state.²⁰ At near-coil state, HI between DNA segments is very strong and it hinders the unraveling of the chain. However, at more extended state HI between DNA segments becomes much weaker. The reducing HI

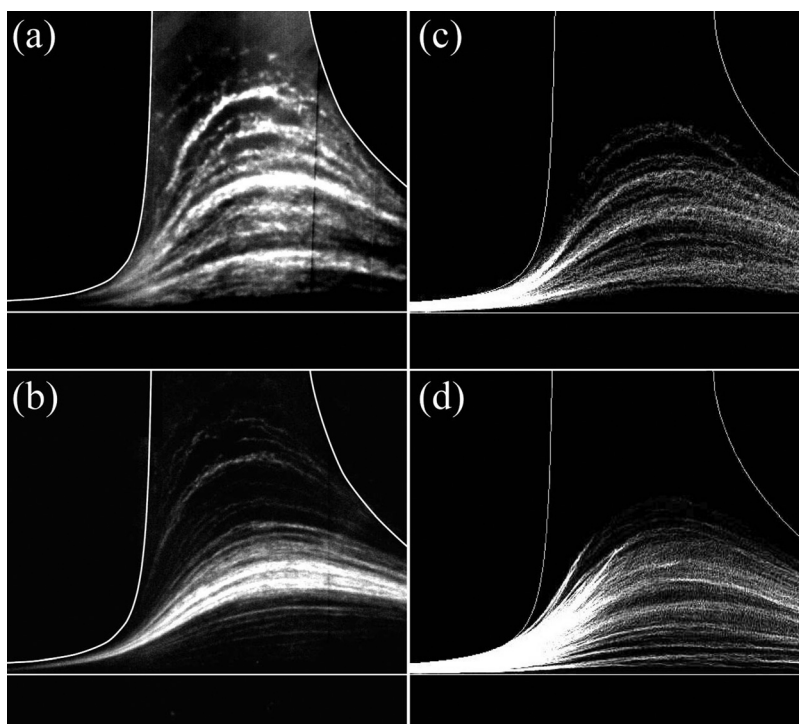


FIG. 6. The time-lapse images of DNA trajectories in case III. The bright lines are DNA trajectories. (a) and (b) are the experimental images at $De = 5$ and $De = 30$, respectively. The flow direction is pointing from right to left. (c) and (d) are the simulation results also at $De = 5$ and $De = 30$.

increases the apparent drag on the chain and accelerates unraveling of the chain, and thus leads to higher DNA extension at high De .

To explain the second trend, we present the distribution of DNA trajectories in case III from both experiments and simulations. Fig. 6 are the time-lapse image of T4-DNA passing case III at low ($De=5$) and high ($De=30$) flow rate from experiments ((a) and (b)) and simulations ((c) and (d)). The white lines represent DNA trajectories. Because each image contains multiple DNA trajectories, these images reveal the distribution of DNA population as they pass through the device. In Fig. 6(a), DNA trajectories from experiments spread quite evenly at low flow rate despite small depletion zones near side walls. In Fig. 6(b), however, DNA trajectories become concentrated around the center of the channel but depleted near the side walls. On the other hand, DNA trajectories from simulations (Figs. 6(c) and 6(d)) always spread evenly, regardless of the change in the flow rate. Comparing Fig. 6(a) with 6(c), we believe the small depletion zones near side walls are mainly caused by the excluded volume effect between DNA and walls. However, the uneven distribution of DNA population observed in Fig. 6(b) but not in Fig. 6(d) is strong evidence indicating that it is caused by the hydrodynamic interaction between the side wall and DNA. It is well known that hydrodynamic interaction causes DNA to migrate from wall under shear flow, and the migration becomes stronger with increasing shear rate.^{30,36,67} The same depletion zones have also been observed in case II along the curved side walls. As discussed previously, the DNA chains passing near the area about $y=0$ experience lower extension in both case II and case III. Since DNA were mostly depleted from this low extension region in case III in experiments, the average DNA extension in case III naturally exceeds that in case II, resulting in a much more significant performance gap than predicted by the simulations.

CONCLUSIONS

We have simulated T4-DNA behavior in complex flow field generated in microchannels with non-trivial geometry. Although the simulations were performed using BD-FEM without hydrodynamic interaction, the results were found not only able to capture the representative DNA conformations observed in experiments but also reasonably close to the experimental data. The differences between the simulation prediction and experimental measurement were rather insignificant if one consider the neglect of HI in our simulations. We analyze the deviation between simulations and experiments, and found that it can be attributed to the neglect of HI. Considering the huge savings on the computational cost from neglecting HI, we conclude that BD-FEM can be used with care as an efficient and economic designing tool for developing new microfluidic device for DNA manipulation.

ACKNOWLEDGMENTS

The authors thank the National Science Council of Taiwan for supporting this research under the grant of NSC 100-2628-E-002-029-MY2.

- ¹C. H. Lee and C. C. Hsieh, *Biomicrofluidics* 7(1), 014109 (2013).
- ²T. T. Perkins, S. R. Quake, D. E. Smith, and S. Chu, *Science* 264(5160), 822–826 (1994).
- ³T. T. Perkins, D. E. Smith, R. G. Larson, and S. Chu, *Science* 268(5207), 83–87 (1995).
- ⁴D. E. Smith, T. T. Perkins, and S. Chu, *Macromolecules* 29(4), 1372–1373 (1996).
- ⁵T. T. Perkins, D. E. Smith, and S. Chu, *Science* 276(5321), 2016–2021 (1997).
- ⁶S. R. Quake, H. Babcock, and S. Chu, *Nature* 388(6638), 151–154 (1997).
- ⁷D. E. Smith and S. Chu, *Science* 281(5381), 1335–1340 (1998).
- ⁸D. E. Smith, H. P. Babcock, and S. Chu, *Science* 283(5408), 1724–1727 (1999).
- ⁹C. M. Schroeder, H. P. Babcock, E. S. G. Shaqfeh, and S. Chu, *Science* 301(5639), 1515–1519 (2003).
- ¹⁰A. Balducci, P. Mao, J. Y. Han, and P. S. Doyle, *Macromolecules* 39(18), 6273–6281 (2006).
- ¹¹C. C. Hsieh, A. Balducci, and P. S. Doyle, *Macromolecules* 40(14), 5196–5205 (2007).
- ¹²C. C. Hsieh, A. Balducci, and P. S. Doyle, *Nano Lett.* 8(6), 1683–1688 (2008).
- ¹³Y. L. Chen, M. D. Graham, J. J. de Pablo, G. C. Randall, M. Gupta, and P. S. Doyle, *Phys. Rev. E* 70(6), 060901 (2004).
- ¹⁴A. Balducci, C. C. Hsieh, and P. S. Doyle, *Phys. Rev. Lett.* 99(23), 238102 (2007).
- ¹⁵C. C. Hsieh and P. S. Doyle, *Korea-Aust. Rheol. J.* 20(3), 127–142 (2008).
- ¹⁶J. O. Tegenfeldt, C. Prinz, H. Cao, S. Chou, W. W. Reisner, R. Riehn, Y. M. Wang, E. C. Cox, J. C. Sturm, P. Silberzan, and R. H. Austin, *Proc. Natl. Acad. Sci. U.S.A.* 101(30), 10979–10983 (2004).

- ¹⁷W. Reisner, K. J. Morton, R. Riehn, Y. M. Wang, Z. N. Yu, M. Rosen, J. C. Sturm, S. Y. Chou, E. Frey, and R. H. Austin, *Phys. Rev. Lett.* **94**(19), 196101 (2005).
- ¹⁸M. D. Graham, *Annu. Rev. Fluid Mech.* **43**, 273–298 (2011).
- ¹⁹C. C. Hsieh, L. Li, and R. G. Larson, *J. Non-Newton. Fluid Mech.* **113**(2–3), 147–191 (2003).
- ²⁰C. C. Hsieh and R. G. Larson, *J. Rheol.* **48**(5), 995–1021 (2004).
- ²¹C. C. Hsieh and R. G. Larson, *J. Rheol.* **49**(5), 1081–1089 (2005).
- ²²C. M. Schroeder, R. E. Teixeira, E. S. G. Shaqfeh, and S. Chu, *Macromolecules* **38**(5), 1967–1978 (2005).
- ²³R. E. Teixeira, H. P. Babcock, E. S. G. Shaqfeh, and S. Chu, *Macromolecules* **38**(2), 581–592 (2005).
- ²⁴D. R. Tree, Y. Wang, and K. D. Dorfman, *Biomicrofluidics* **7**(5), 054118 (2013).
- ²⁵Y. L. Chen, *Biomicrofluidics* **7**(5), 054119 (2013).
- ²⁶W. F. Reinhart, D. R. Tree, and K. D. Dorfman, *Biomicrofluidics* **7**(2), 024102 (2013).
- ²⁷R. G. Larson, *J. Rheol.* **49**(1), 1–70 (2005).
- ²⁸C. C. Hsieh, S. J. Park, and R. G. Larson, *Macromolecules* **38**(4), 1456–1468 (2005).
- ²⁹J. M. Kim and P. S. Doyle, *J. Chem. Phys.* **125**(7), 074906 (2006).
- ³⁰R. M. Jendrejack, E. T. Dimalanta, D. C. Schwartz, M. D. Graham, and J. J. de Pablo, *Phys. Rev. Lett.* **91**(3), 038102 (2003).
- ³¹R. M. Jendrejack, D. C. Schwartz, M. D. Graham, and J. J. de Pablo, *J. Chem. Phys.* **119**(2), 1165–1173 (2003).
- ³²Y. L. Chen, M. D. Graham, J. J. de Pablo, K. Jo, and D. C. Schwartz, *Macromolecules* **38**(15), 6680–6687 (2005).
- ³³Y. Zhang, J. J. de Pablo, and M. D. Graham, *J. Chem. Phys.* **136**(1), 014901 (2012).
- ³⁴J. Rotne and S. Prager, *J. Chem. Phys.* **50**(11), 4831–4837 (1969).
- ³⁵N. Liron and S. Mochon, *J. Eng. Math.* **10**(4), 287–303 (1976).
- ³⁶L. Fang, C. C. Hsieh, and R. G. Larson, *Macromolecules* **40**(23), 8490–8499 (2007).
- ³⁷S. Chen and G. D. Doolen, *Annu. Rev. Fluid Mech.* **30**, 329–364 (1998).
- ³⁸A. Malevanets and R. Kapral, *J. Chem. Phys.* **110**(17), 8605–8613 (1999).
- ³⁹A. Lamura, G. Gompper, T. Ihle, and D. M. Kroll, *Europhys. Lett.* **56**(3), 319–325 (2001).
- ⁴⁰G. Gompper, T. Ihle, D. M. Kroll, and R. G. Winkler, *Adv. Polym. Sci.* **221**, 1–87 (2009).
- ⁴¹O. B. Usta, J. E. Butler, and A. J. C. Ladd, *Phys. Fluids* **18**(3), 031703 (2006).
- ⁴²N. Watari, M. Makino, N. Kikuchi, R. G. Larson, and M. Doi, *J. Chem. Phys.* **126**(9), 094902 (2007).
- ⁴³Y. L. Chen, H. Ma, M. D. Graham, and J. J. de Pablo, *Macromolecules* **40**(16), 5978–5984 (2007).
- ⁴⁴X. Hu, S. N. Wang, and L. J. Lee, *Phys. Rev. E* **79**(4), 041911 (2009).
- ⁴⁵W. C. Liao, X. Hu, W. X. Wang, and L. J. Lee, *Biomicrofluidics* **7**(3), 034103 (2013).
- ⁴⁶A. Mohan and P. S. Doyle, *Macromolecules* **40**(24), 8794–8806 (2007).
- ⁴⁷J. Ou, J. Cho, D. W. Olson, and K. D. Dorfman, *Phys. Rev. E* **79**(6), 061904 (2009).
- ⁴⁸J. Cho and K. D. Dorfman, *J. Chromatogr. A* **1217**(34), 5522–5528 (2010).
- ⁴⁹J. Cho, S. Kumar and K. D. Dorfman, *Electrophoresis* **31**(5), 860–867 (2010).
- ⁵⁰C. C. Zuo, F. Ji, and Q. Q. Cao, *Polymer* **50**(22), 5326–5332 (2009).
- ⁵¹Z. Chun-Cheng, J. Feng, C. Qian-Qian, and Y. Jing-Song, *Polymer* **49**(3), 809–815 (2008).
- ⁵²D. W. Trahan and P. S. Doyle, *Biomicrofluidics* **3**(1), 12803 (2009).
- ⁵³K. D. Dorfman, S. B. King, D. W. Olson, J. D. P. Thomas, and D. R. Tree, *Chem. Rev.* **113**(4), 2584–2667 (2013).
- ⁵⁴J. M. Kim and P. S. Doyle, *Lab Chip* **7**(2), 213–225 (2007).
- ⁵⁵C. C. Hsieh and T. H. Lin, *Biomicrofluidics* **5**(4), 044106 (2011).
- ⁵⁶C. C. Hsieh, T. H. Lin, and C. D. Huang, *Biomicrofluidics* **6**(4), 044105 (2012).
- ⁵⁷Z. Chen and K. D. Dorfman, “Comparison of microfabricated hexagonal and lamellar post arrays for DNA electrophoresis,” *Electrophoresis* (in press).
- ⁵⁸J. Tang, N. Du, and P. S. Doyle, *Proc. Natl. Acad. Sci. U. S. A.* **108**(39), 16153–16158 (2011).
- ⁵⁹D. Long, J. L. Viovy, and A. Ajdari, *J. Phys.-Condens. Matter* **8**(47), 9471–9475 (1996).
- ⁶⁰K. Jo, Y. L. Chen, J. J. de Pablo, and D. C. Schwartz, *Lab Chip* **9**(16), 2348–2355 (2009).
- ⁶¹N. P. Teclamarium, V. A. Beck, E. S. G. Shaqfeh, and S. J. Muller, *Macromolecules* **40**(10), 3848–3859 (2007).
- ⁶²P. T. Underhill and P. S. Doyle, *J. Non-Newton. Fluid Mech.* **122**(1–3), 3–31 (2004).
- ⁶³R. G. Larson, T. T. Perkins, D. E. Smith, and S. Chu, *Phys. Rev. E* **55**(2), 1794–1797 (1997).
- ⁶⁴R. M. Jendrejack, J. J. de Pablo, and M. D. Graham, *J. Chem. Phys.* **116**(17), 7752–7759 (2002).
- ⁶⁵D. M. Heyes and J. R. Melrose, *J. Non-Newton. Fluid Mech.* **46**(1), 1–28 (1993).
- ⁶⁶A. Balducci and P. S. Doyle, *Macromolecules* **41**(14), 5485–5492 (2008).
- ⁶⁷R. M. Jendrejack, D. C. Schwartz, J. J. de Pablo, and M. D. Graham, *J. Chem. Phys.* **120**(5), 2513–2529 (2004).